ResearchGate

See discussions, stats, and author profiles for this publication at: https://www.researchgate.net/publication/386567717

Closed-Loop Stall Control using Pulsed-DBD Plasma Actuation

Preprint · December 2024

DOI: 10.13140/RG.2.2.22995.90406

CITATIONS

0

3 authors, including:

David Greenblatt

Technion – Israel Institute of Technology

199 PUBLICATIONS **5,279** CITATIONS

SEE PROFILE

All content following this page was uploaded by David Greenblatt on 09 December 2024.

The user has requested enhancement of the downloaded file.

Closed-Loop Stall Control using Pulsed-DBD Plasma Actuation

Mordechai Garcia,[*]
Technion – Israel Institute of Technology, Technion City, Haifa 3200003, Israel

Michael Mongin[†]
U.S. Air Force Research Laboratory, Wright-Patterson Air Force Base, OH 45433

David Greenblatt[‡]
Technion – Israel Institute of Technology, Technion City, Haifa 3200003, Israel

A closed-loop stall control system, employing pulsed-DBD plasma actuators, was implemented on the semi-span wing of a 6:1 scale general aviation aircraft model, and evaluated in a wind tunnel. Sensing of incipient stall was achieved by means of pressure ports located just below the leading-edge, inspired by conventional scoop-type pneumatic stall-warning systems. While negative pressure at the scoop orifice draws air though the reed of a horn, to warn the pilot of incipient stall, the present system relies on the pressure zero-crossings to either initiate or terminate plasma pulsations. Decreasing- or increasing-pressure zero-crossings, corresponding to pitch-up or pitch-down, either initiated or terminated pulsations, respectively. Lift and drag coefficient results, based on closed-loop control, were compared with open loop (continuous) plasma pulsations under static and dynamic—harmonic and pitch-and-hold—angle-of-attack variations. Under all light, moderate and deep stall scenarios, at a wide range of reduced frequencies, negligible differences were observed between open- and closed-loop control, thereby demonstrating the viability of the closed-loop system. With increasing pitchrate, the angles-of-attack corresponding to pitch-down zero-crossings increased successively, to angles greater than the static stall angle. This had no measurable effect on the results because the timescales governing boundary layer separation were at least an order-of-magnitude larger than the time-intervals between the zero-crossing angle and the static stall angle. DBD plasma actuators can easily be retrofitted to general aviation aircraft, that incorporate scoop-type stall warning systems, and the next step should be to evaluate the system on a full-scale wing, or in flight.

Nomenclature

AR	=	aspect ratio, $b/\bar{c}$
$b/2$	=	wing semi-span (m)
$\bar{c}$	=	average wing chord (m)
C_D	=	drag coefficient, $F_D / q_\infty S$
C_{D0}	=	zero-lift base-drag coefficient
C_L	=	lift coefficient, $F_L / q_\infty S$
f	=	airfoil oscillation frequency (Hz)
f_{ion}	=	plasma ionization frequency (Hz)
f_p	=	plasma pulse-modulation frequency (Hz)
F^+	=	blade reduced frequency, $f_p \bar{c} / U_\infty$
k	=	reduced oscillation frequency, $\omega \bar{c} / 2U_\infty$
q_∞	=	dynamic pressure, $\frac{1}{2}\rho U_\infty^2$ (Pa)
Re	=	Reynolds number, $U_\infty \bar{c} / \nu$
S	=	wing planform area (m^2)

[*] Graduate Student, Faculty of Mechanical Engineering.
[†] Aerospace Researcher, Aerospace Systems Directorate, AIAA Young Professional Member.
[‡] Professor, Louis and Helen Rogow Chair in Aeronautical Engineering. Faculty of Mechanical Engineering, AIAA Associate Fellow, davidg@technion.ac.il (corresponding author).

U_∞ = wind tunnel freestream velocity (m/s)
V = voltage (V)
V_{pp} = peak-to-peak voltage (kV)
α = angle-of-attack (°)
α_s = stall angle-of-attack (°)
ω = airfoil circular oscillation frequency (rad/s)

I. Introduction

Stall on fixed-wing aircraft occurs when the angle-of-attack exceeds a critical value, denoted by the stall angle α_s, and is characterized by a loss of lift and, in many cases, control. On conventional subcritical unswept wings, stall is initiated by boundary layer separation from the surface that results from a pressure rise along the chord. Conventional flight is generally restricted to flight speeds that exceed the corresponding stall speed; for example, during takeoff and landing, typical safety regulations demand a minimum flight speed that is 20% higher than the stall speed [1]. This allows pilots or automatic flight controllers to avoid stall, but this not always the case. Two recent surveys found that wing stall still accounts for approximately 12% of general aviation (GA) accidents, and that fatalities resulting from stall-induced accidents during the last six decades have remained consistently high at 39%. [2-4].

In addition to improvements in flight training, researchers have for many years attempted to render wings resistant to stall. This can be done via design of the profile or planform [5] or by some sort of flow separation control device. The most common and widely used stall control device is the vortex generator (VG) [6,7]. VGs are small vanes that are attached to the wing in an oblique manner, often in symmetric pairs, and produce streamwise vortices that transport high-momentum flow towards the surface, rendering the flow less prone to separation. They can be, and often are, retrofit to aircraft wings and flaps, but they only operate in a narrow band of flight conditions which limits control authority, and they add drag at cruise conditions [6,7]. The latter can be offset by developing "on demand" VGs, for example, deployable VGs using Shape Memory Alloys (SMAs) [8,9] or rotatable VGs using servo motors [10]. However, this does not solve the problem of control authority, and for this we must turn to active flow control (AFC) methods.

Many AFC techniques, such as slot blowing [11], synthetic jets [12], or fluidic vortex generators [13] are known to be effective for stall control. However, they require major wing design modifications and add significant system complexity. A relatively simple and well-known device is the dielectric barrier discharge (DBD) plasma actuator [14]. It consists of a dielectric material and two electrodes—one encapsulated and one exposed—arranged asymmetrically. DBD actuators can be integrated into the profile geometry [15] or attached to the surface using an adhesive [16]. An Alternating Current (AC) waveform, from a few kilovolts to tens of kilovolts V_{pp}, is typically applied to the electrodes in the ionization frequency range $f_{\text{ion}} = \mathcal{O}(10^3)$ to $\mathcal{O}(10^4)$ Hz, between the electrodes. Pulse-modulation of the ionization frequency at a lower frequency f_p achieves two objectives. First, it is selected to correspond to a known flow instability that is receptive to active perturbations; and second, it can be operated at a very low duty cycle d.c., even a few percent, which results in a proportional power saving [17]. When attached to the leading-edge of an airfoil or wing, actuation can either delay flow separation to higher angles-of-attack or attach an otherwise separated flow. Actuation usually produces a modest increase in $C_{L,\max}$ and a significant increase in post-stall C_L (see references in [16]), essentially preventing leading-edge stall up to large post-stall angles of attack. Excitation of the airfoil separation bubble or the freestream shear layer is commonly characterized by the reduced frequency:

$$F^+ \equiv \frac{f_p c}{U_\infty} \tag{1}$$

It has been determined empirically that the excitation is effective for lift enhancement over the range $0.3 \lesssim F^+ \lesssim 5$ [12] and up to large post-stall angles of attack. Reduced frequencies up to $F^+ = 50$ are also effective, but they have proportionally higher power consumption and a smaller effect on lift hysteresis at deep stall angles of attack [18].

For purposes of implementation and optimization, DBD plasma actuators should not be pulsed continuously; rather, they should only be initiated when the aircraft is at, or close to, stall. Hence, at least one sensor must be deployed, within a closed-loop control system, to provide feedback for initiation and termination, as necessary. A closed-loop DBD plasma control scheme was developed by [19] based on measuring the upper surface pressure signal downstream $(x/c = 8\%)$ of the actuator. The actuator was operated at a low-amplitude pulsation mode—designed to amplify disturbances at incipient stall—and then switched to a high-amplitude separation control mode when some bandpass filtered threshold was exceeded. The control scheme was demonstrated for both statically and dynamically pitching airfoils, under both light and deep dynamic stall. In a different approach, flush-mounted microphones near the upper surface trailing-edge of an airfoil were used to detect incipient separation by [10]. The microphone signals were processed by acquiring multiple data sets and computing their bandwidth-limited power spectral densities (PSDs) at each angle of attack. A location on the airfoil surface was identified where the integrated PSD power increased markedly at incipient stall.

A far older and simpler way of detecting incipient stall is based on stagnation-point movement just below the leading-edge [20], which typically uses a pneumatic or mechanical system. In pneumatic systems, the stagnation point crosses over an orifice (the scoop), and the resulting negative air pressure sucks air through a reed, producing an audible warning. For mechanical systems, typically a vane (or tab) is deflected upward as the stagnation point crosses over it, to produce an electrically driven audible warning. The global objective of our research is to develop a closed-loop stall control system based on existing scoop hardware used on many GA aircraft. The scope of research presented in this paper involves wind tunnel experiments, performed on scale model semi-span wing configuration of a popular aircraft. Pressure ports below the leading-edge, representative of a scoop orifice, are used to test a simple closed-loop DBD plasma stall control system, for initiation and termination of the pulsations. The basic strategy is developed on the basis of static wing measurements, and then the system is tested dynamically at a wide range of angles-of-attack and pitchrates. Both harmonic angle-of-attack oscillations, as well as pitch-and-hold angle-of-attack variations are considered.

II. Experimental Setup

A starboard wing, constructed from expanded polyolefin (EPO)—from a battery-powered FMS Ranger PNP radio controlled (RC) model—was employed for the experiments. The wing has a constant chord-length inboard (root) section, a mildly tapered outboard section, with drooped wingtips, and is based on a 6:1 Cessna 172 wing planform, with a semi-span (not including the model body) of 1,620 mm. The wing profile was determined by digitizing the root coordinates and then comparing them to a large airfoil database. The comparison was based on minimizing the sum of the squared deviations between the digitized geometry and the database geometries, allowing for both rotation and linear scaling in x/c and z/c coordinate directions. The closest match, i.e., the minimum sum of the squared differences, was to a GOE 702 airfoil, whose thickness is scaled by a factor of 0.6702 (see Fig. 1).

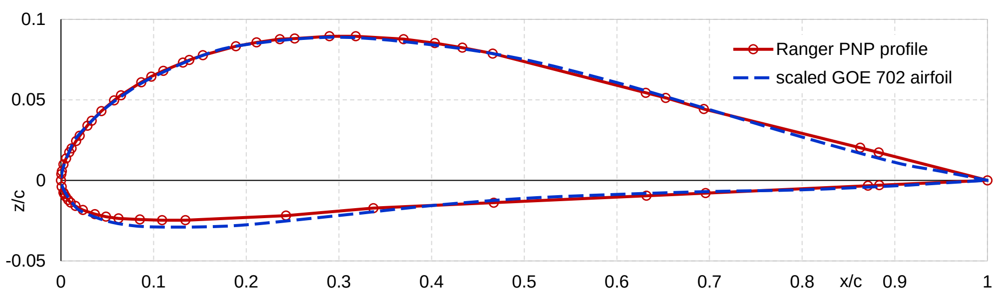

Fig. 1. Ranger wing root profile compared with a GOE 702 airfoil, scaled in the *z/c* coordinate direction by a factor of 0.6702. Note that *x/c* and *z/c* scales are different.

In our previous research [21], open-loop full body wind tunnel and flight experiments were performed with DBD plasma actuators. In this research, identical actuators, constructed using 50 μm thick copper electrodes and a 0.4 mm thick silicone rubber dielectric, were mounted along the full extent of the span (see Fig. 2). High-voltage signals were supplied by means of a commercially available Minipuls 0.1® (GBS Elektronik) generator with a 12-kV peak-to-peak capability in the frequency range 5 to 20 kHz, previously used for flight experiments [21]. The assembly consists of a full bridge converter and a transformer cascade, with a total mass of 360 grams. Power is supplied by an 11.1-volt lithium-polymer battery, via a 30-volt step-up boost converter. Burst frequency f_p, duty cycle d.c. and phase are preset by board-mounted trimpots. Plasma voltage and pulsation frequency were monitored using a Testec ESTEC HVP-15HF high voltage probe. The high-voltage wiring was glued to the wing-strut and was inserted into grooves on the lower surface of the wing as illustrated in Fig. 2.

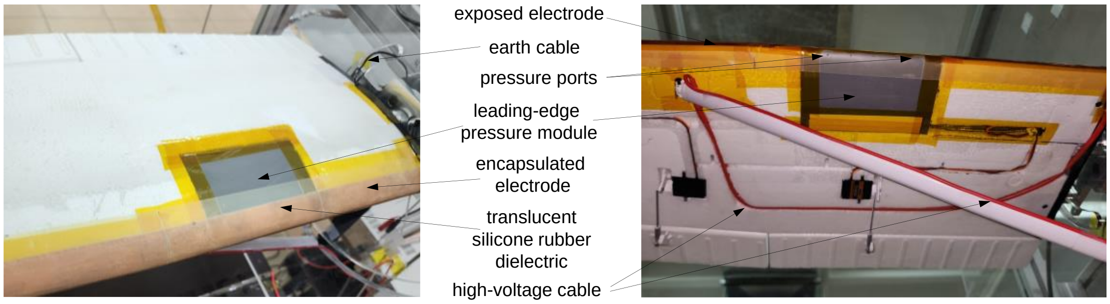

Fig. 2. Left: Photograph from above the wing, showing the pressure module, encapsulated electrode, translucent silicone dielectric and earth wiring. Right: Photograph from below the wing, showing the pressure ports on the pressure module, exposed electrode and high-voltage AC wiring.

For stall sensing based on the scoop-system described in section I, a 3-D printed (MSLA resin) section of the leading-edge was replaced by a leading-edge pressure module incorporating five pressure ports and an internal cavity (see Fig. 2 and Fig. 3). The module geometry was obtained from the digitized profile coordinates shown in Fig. 1, with pressure ports staggered along the span, corresponding to the chordwise range $0.32\% \leq x/c \leq 1.1\%$, as illustrated in Fig. 3 (left). The ports were attached to five Honeywell HSC 250 pascal differential pressure sensors that were located inside module cavity Fig. 3 (right). The reference pressures were attached to a common plenum which, in turn, was connected to the static line of the tunnel pitot-static tube.

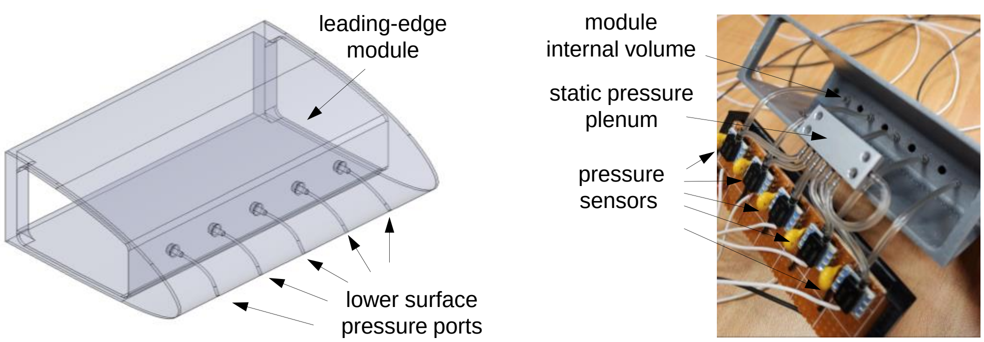

Fig. 3. Left: Transparent CAD rendering showing five pressure port located on the pressure module lower surface. Right: photograph of the module cavity prior to installation, showing the pressure sensors and plenum.

Wind tunnel experiments were performed in a blow-down open wind tunnel, driven by a 75kW blower, where the original 1.0 × 0.61 m nozzle [22] was replaced with a 1.0 × 1.9 m nozzle and test section. This new configuration has a maximum wind speed of $U_\infty = 16$ m/s, a maximum flow distortion of 2.5% and a maximum turbulence intensity of 0.5%. The wind tunnel speed was measured using a pitot-static probe, mounted upstream of the model, using a Siemens QBM3020-1U pressure transducer, together with an E+E Elektronik EE211 humidity and temperature. The wing was mounted horizontally in the test section on a 20×80 mm aluminum profile, incorporating a stainless-steel shaft mounted on bearings, a six-component ATI Delta SI-330-30 aerodynamic balance, an extension, a lever-arm and a wing adapter (see Fig. 4, left). A Nema 17 stepper motor was also fixed to the aluminum profile and attached to the shaft via a timing belt. Using micro stepping and gear ratios, step resolution ranged from 0.9 to 0.014 degrees. The pitch angle was measured using a Singer Instruments Model MTS-D inclinometer. To mitigate wall boundary layer effects, the wing was located 15 cm from the test section wall, and an 80×80 cm Plexiglas endplate placed at approximately 1.5 mm from the wing root. The wing adapter comprised two components, namely, an aluminum component with a central rod with two (fore and aft) locating bars (Fig. 4, right), and a 3D printed section designed to replicate the wing-body connection. Slots were machined on the endplate to facilitate rotational motion of the locating bars, and an additional slot was machined to allow connection of the wing-strut to the lever arm (Fig. 4, right). Both static experiments and two types of dynamic experiments were performed, namely, harmonic oscillations and pitch-and-hold motions. Pitch-and-hold motions were based on phase-shifted half-sine-wave motions, followed by a constant angle-of-attack.

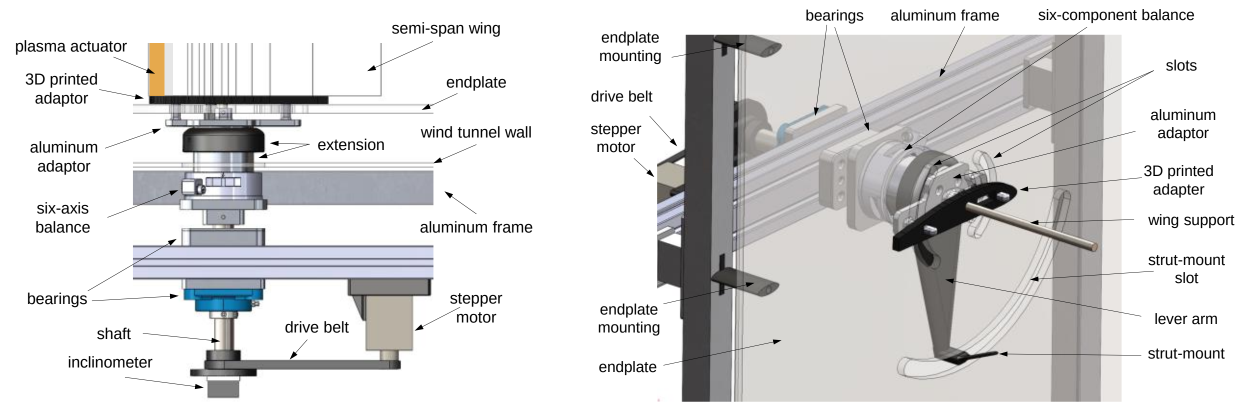

Fig. 4. Left: Partial top view schematic of the cantilever setup, showing the main assembly components required for pitching the wing and measuring the pitch angle. Right: Schematic of the assembly from inside the test section with the wing removed.

III. Discussion of Results

A. Static Load Data and Sensing

Static pitching experiments were conducted by simultaneously measuring the airfoil loads and the five lower-surface leading-edge pressures from the ports on the leading-edge module. Both wind-on at $U_\infty = 8.5$ m/s $(Re \equiv U_\infty \bar{c} / \nu = 1.5\times10^5)$ and wind-off (tare) load experiments were performed by pitching the airfoil from $\alpha = -10°$ to $+30°$ in steps of 0.45°. Data were acquired at a rate of 10^4 samples per second for 0.25 seconds, i.e., $\tau \equiv tU_\infty / \bar{c} = 8.5$, with a delay of 1.75 seconds, i.e., $\tau = 60$. At each angle, the data were averaged and the tare was removed to produce the net aerodynamic loads, which were subsequently non-dimensionalized with the dynamic pressure and planform area to obtain the wing lift and drag coefficients: $C_L \equiv L / q_\infty S$ and $C_D \equiv D / q_\infty S$.

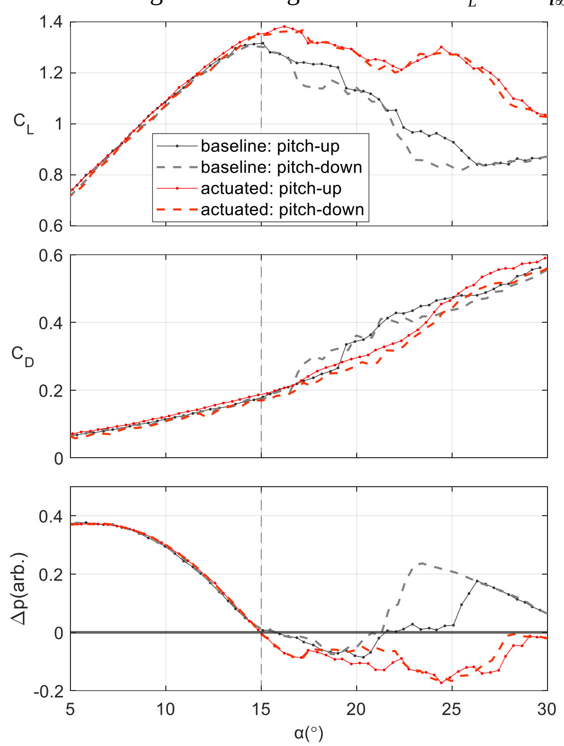

Fig. 5. Lift and drag coefficient results, together with corresponding leading-edge stall pressure under static pitch-up and pitch-down motions, for baseline and continuously pulse-modulated $(F^+ = 3.3)$ cases, at $Re = 1.5\times10^5$.

Fig. 5 shows both static pitch-up and pitch-down for baseline and plasma actuation results under conditions similar to those selected for the full model and flight experiments, namely $f_p = 110$ Hz, $U_\infty = 8.5$ m/s ($F^+ = 3.3$) and $\text{d.c.} = 15\%$. The baseline lift and drag coefficient results are qualitatively comparable to the full model results, where tailing-edge separation is observed on the inboard part of the wing using tufts [21]. Static stall occurs at $\alpha_s \approx 15.5°$, with inboard leading-edge separation at $\alpha \approx 19°$, and full-span separation at $\alpha \approx 27°$. In comparison to the full model results, there are two main differences due to the absence of the body and empennage. First, the baseline $C_{L,\max}$ and α_s are approximately 0.1 and 2° lower, respectively; and, second the base-drag ($C_{D0} \equiv C_{D,L=0}$) is 0.03 compared to 0.11 on the full scale model (not explicitly visible on the figure). With plasma actuation, the results are again comparable to those of the full model, namely, a small increase in $C_{L,\max}$, and effective elimination of bi-stable behavior. There are, however, two exceptions. First, plasma actuation produces an increase in $C_{L,\max}$ of approximately 0.070, versus 0.025 in the case of the full model; and second, post-stall C_L does not drop below the actuated $C_{L,\max}$. These effects are mainly due to the body, which produces increasing lift with angle of attack, attaining a maximum at $\alpha \approx 45°$.

With increasing angle-of-attack, the lower surface pressure at $x/c = 0.32\%$ (shown in Fig. 5 as a voltage) has a gentle peak at $\alpha \approx 5°$, corresponding to the stagnation point, and decreases with further increasing angle-of-attack. The similarity between the baseline and open-loop controlled cases is consistent with the negligible effect on wing circulation. Further increases in angle-of-attack result in a zero-crossing of the baseline pressure, corresponding to half a degree lower than α_s; thus, the zero-crossing is more an indicator of stall than a stall warning. The other four pressure sensors did not produce zero crossings (not shown) and were therefore not used. Placing a pressure port further upstream proved to be impractical due to the presence of the actuator exposed electrode. At $\alpha \approx 22°$, the baseline pressure again goes positive due to localized leading-edge stall, that produces upstream movement of the stagnation point. With actuation, as expected, no meaningful pre-stall effect is observed on either the aerodynamic coefficients or the leading-edge pressure. However, the leading-edge pressure remains negative at least up to the limits of our considered range, i.e., $\alpha_{\max} = 30°$, because it prevents full leading-edge stall. Due to the near correspondence of the zero-crossing and the static stall angle, the sensor placement at $x/c = 0.32\%$ was deemed suitable for implementation in a simple closed-loop system.

B. Closed-Loop Control Scheme

Based on the above results, a simple closed-loop scheme was implemented with three fixed inputs, namely: a threshold pressure p_t, the reduced frequency F^+, and the average chord-length $\bar{c}$. The freestream velocity is measured using the tunnel Pitot-static probe, and thereby facilitates the calculation of the pulsation frequency and delay time: $f_p = F^+ U_\infty / \bar{c}$. During the experiments, the pressure signal is averaged in 50 ms windows to obtain Δp. The option of introducing dimensionless time delays for pitch-up and pitch down motion, based on a convective time input $\bar{c}/U_\infty$, was implemented but not employed. Initial experiments were performed with the simplest logic, namely: if $\Delta p \le p_t$ then the Minipuls-0.1 controller is initiated, and it remains so until $\Delta p > p_t$ (see the schematic in Fig. 6). Despite the simplicity, this control logic produced excellent results, described in the sub-sections below.

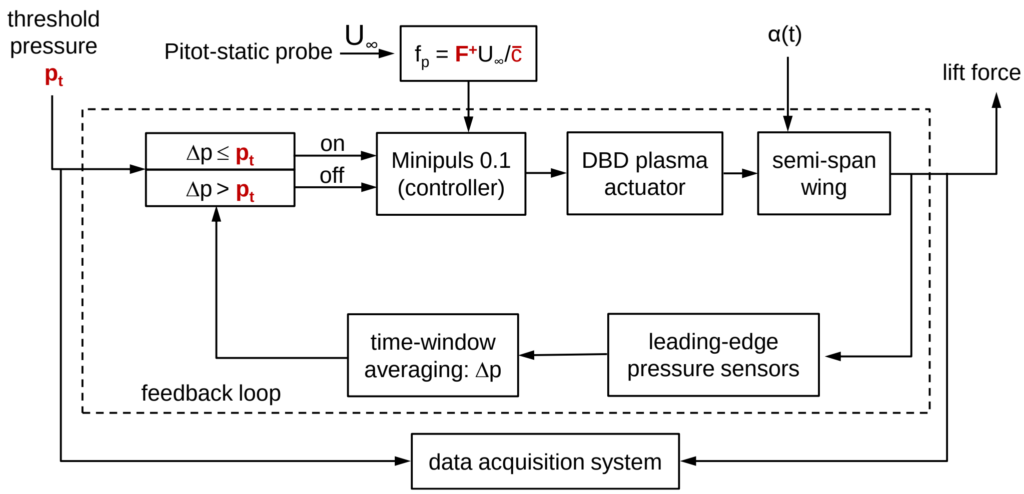

Fig. 6. Simple closed-loop control scheme based on the leading-edge scoop with fixed inputs, namely: threshold voltage p_t, reduced frequency F^+ and average chord-length $\bar{c}$ (all shown in red).

C. Harmonic Airfoil Pitching

Harmonic pitching was conducted under the conditions $\alpha = \bar{\alpha} + 5° \sin \omega t$, at dimensionless pitchrates $k \equiv \omega \bar{c} / 2U_\infty = 0.01$, 0.05 and 0.1, where $\omega = 2\pi f$. Three dynamic stall scenarios were considered, namely, "light" dynamic stall $(\bar{\alpha} = 12°,\ \alpha_{\max} = \alpha_s + 2°)$, "moderate" dynamic stall $(\bar{\alpha} = 15°,\ \alpha_{\max} = \alpha_s + 5°)$, and "deep" dynamic stall $(\bar{\alpha} = 18°,\ \alpha_{\max} = \alpha_s + 8°)$. Both wind-on $(U_\infty = 8.5 \text{ m/s})$ and wind-off at the same $\bar{\alpha}$ and f (dynamic tare) experiments were performed. Harmonic pitching load and pressure data were acquired at 10^4 samples per second, where data for each cycle were binned into time-intervals of $\Delta t = 1/200 f$ and averaged. The data were low-pass filtered below 13 Hz, to eliminate two resonant modes corresponding to vertical and horizonal wind flapping at 13 Hz and 25 Hz, respectively. Each experiment included a minimum of 10 cycles, which were subsequently phase-averaged and subtracted from the tare data to produce the net aerodynamic loads.

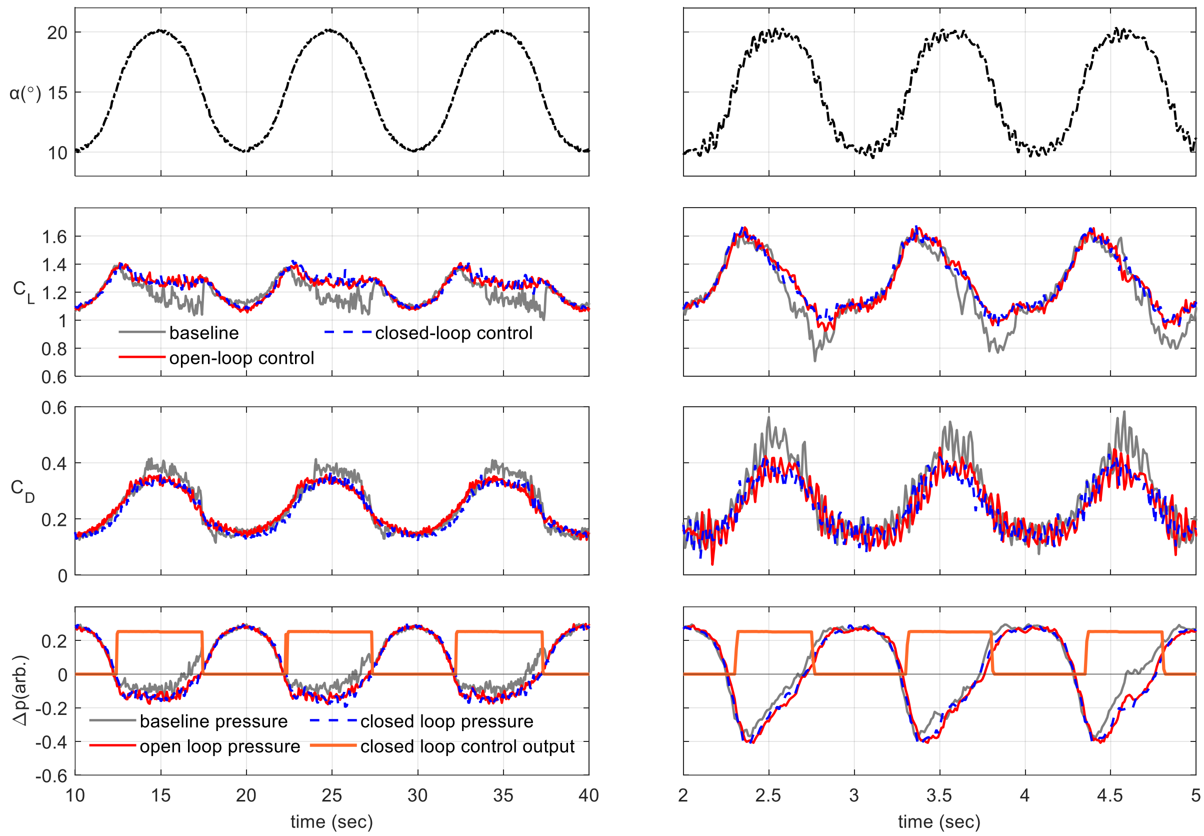

Fig. 7. Time-based illustration of the closed-loop control scheme for moderate stall with $\bar{\alpha} = 15°$ at $k = 0.01$ (left) and $k = 0.1$ (right). Each data point is obtained by averaging 200 raw data points in successive time-windows.

An example of the online data processing and application of the closed-loop scheme on a time basis are shown in Fig. 7, for $\bar{\alpha} = 15°$ (moderate dynamic stall) for two pitchrates, namely $k = 0.01$ and 0.1, showing angle-of-attack, lift coefficient, leading-edge pressure and the actuation signal. The threshold pressure $p_t = 0$ was selected, based on the results in Fig. 5. The open-loop label denotes continuous pulse-modulation, while the closed-loop label denotes pulse-modulation initiation for $\Delta p \le 0$ and termination for $\Delta p > 0$. As expected, lift coefficients associated with either open- or closed-loop control produce slightly large maximum values and increases in post stall lift that depend on pitchrate. The unsteady oscillations observed at post-stall angles of attack are also noticeably smaller, for both reduced frequencies. The differences between open- and closed-loop control are far smaller, and difficult to quantify precisely due to the relatively large associated scatter. The closed-loop control algorithm, implemented using LabVIEW, was not developed using real-time computing and therefore there is a 20 to 50 millisecond deadtime between zero pressure crossings and initiation or termination of pulsations, due to data acquisition and time-window averaging. This dead-time had only a minor effect on the efficacy of the closed-loop system, as described below.

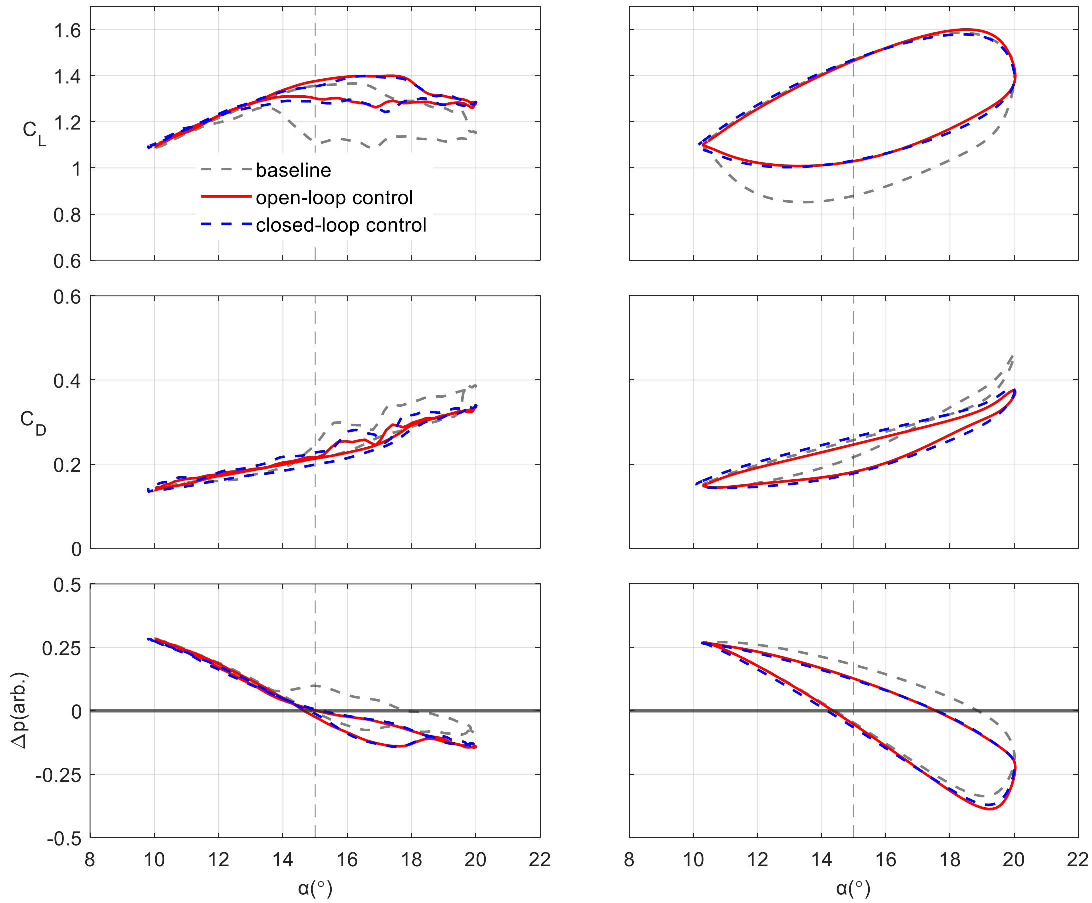

Fig. 8. Phase-averaged baseline, open-loop and closed-loop aerodynamic coefficients and leading-edge pressure with $\bar{\alpha} = 15°$ at $k = 0.01$ (left) and $k = 0.1$ (right).

Data from Fig. 7 was phase-averaged over 10 and 18 cycles, respectively, and the results are presented in Fig. 8 on the basis of angle-of-attack. Additional representative cases, corresponding to light, moderate and deep stall are shown for the three pitchrates in Fig. 9 to Fig. 11. For the most part, the open- and closed-loop results are similar, with only minor differences between the pitch-up and pitch down motions. In both cases, actuation generally decreases the hysteresis loops, consistent with other studies [18,23], producing higher C_L and lower C_D during the downstroke. Important from a sensing point-of-view is that the leading-edge pressure Δp zero-crossing reduces slightly, by up to 0.5°, due to the well-known lift (circulation) overshoot associated with dynamic pitch-up motion. This desirable effect means that the same sensing logic can be used for both static and dynamic pitching experiments. The pitch-down zero-crossing appeared to pose more of a challenge for the control logic because it increases by between 2° and 3°. However, this did not prove to be a problem for the reasons discussed below.

Additional phase-averaged results under light and deep and stall at $k = 0.05$ are shown in Fig. 9. As in the moderate stall case shown in Fig. 8, there are only minor differences between open- and close-loop results. An uncertainty analysis was carried out, based on the number of cycles, N, where σ_C is the standard deviation associated with each phase-averaged lift or drag coefficient C. Uncertainties based on 95% confidence intervals ($C \pm 2\sigma_C / \sqrt{N}$ 95% CI), are shown for representative points. Note that these uncertainties are conservative because they do not take into account the time-window averaging of the raw lift and drag data. As expected, smaller uncertainties are associated with the pre-static-stall, nominally attached-flow angles of attack (see Fig. 7). The main conclusion that can be drawn is that the differences between open- and closed loop control are most likely due to experimental error.

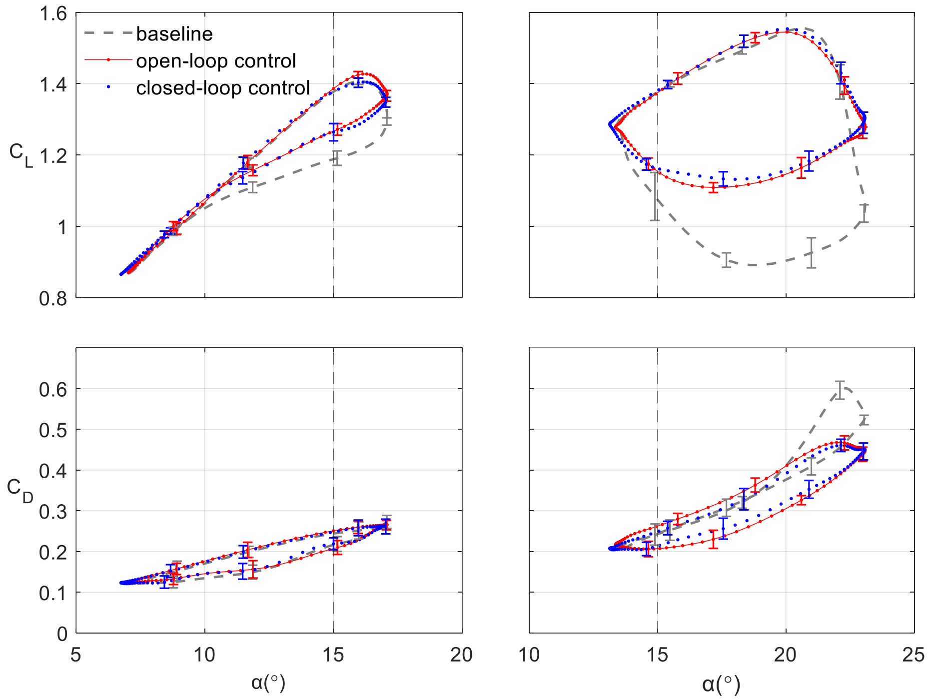

Fig. 9. Phase-averaged baseline, open-loop and closed-loop aerodynamic coefficients with $\bar{\alpha} = 12°$ (left) and $\bar{\alpha} = 18°$ (right) at $k = 0.05$. Error bars at representative locations show the measurement precision with 95% confidence intervals ($\bar{C} \pm 2\sigma_C / \sqrt{N}$ 95% CI).

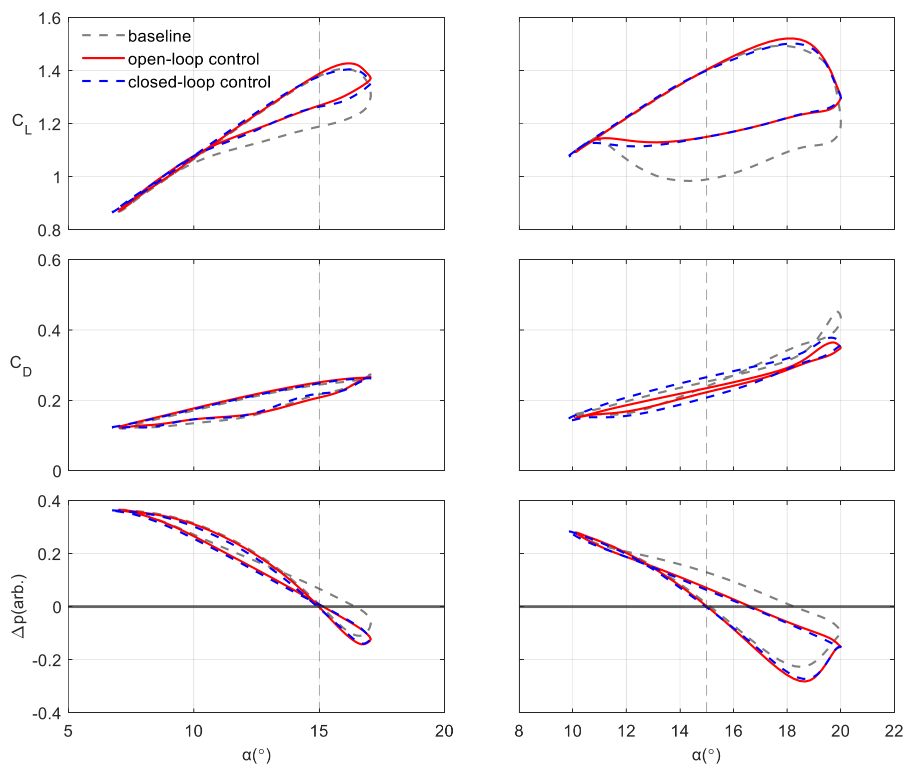

Fig. 10. Phase-averaged baseline, open-loop and closed-loop aerodynamic coefficients and leading-edge pressure at $k = 0.05$, with $\bar{\alpha} = 12°$ (left) and $\bar{\alpha} = 15°$ (right).

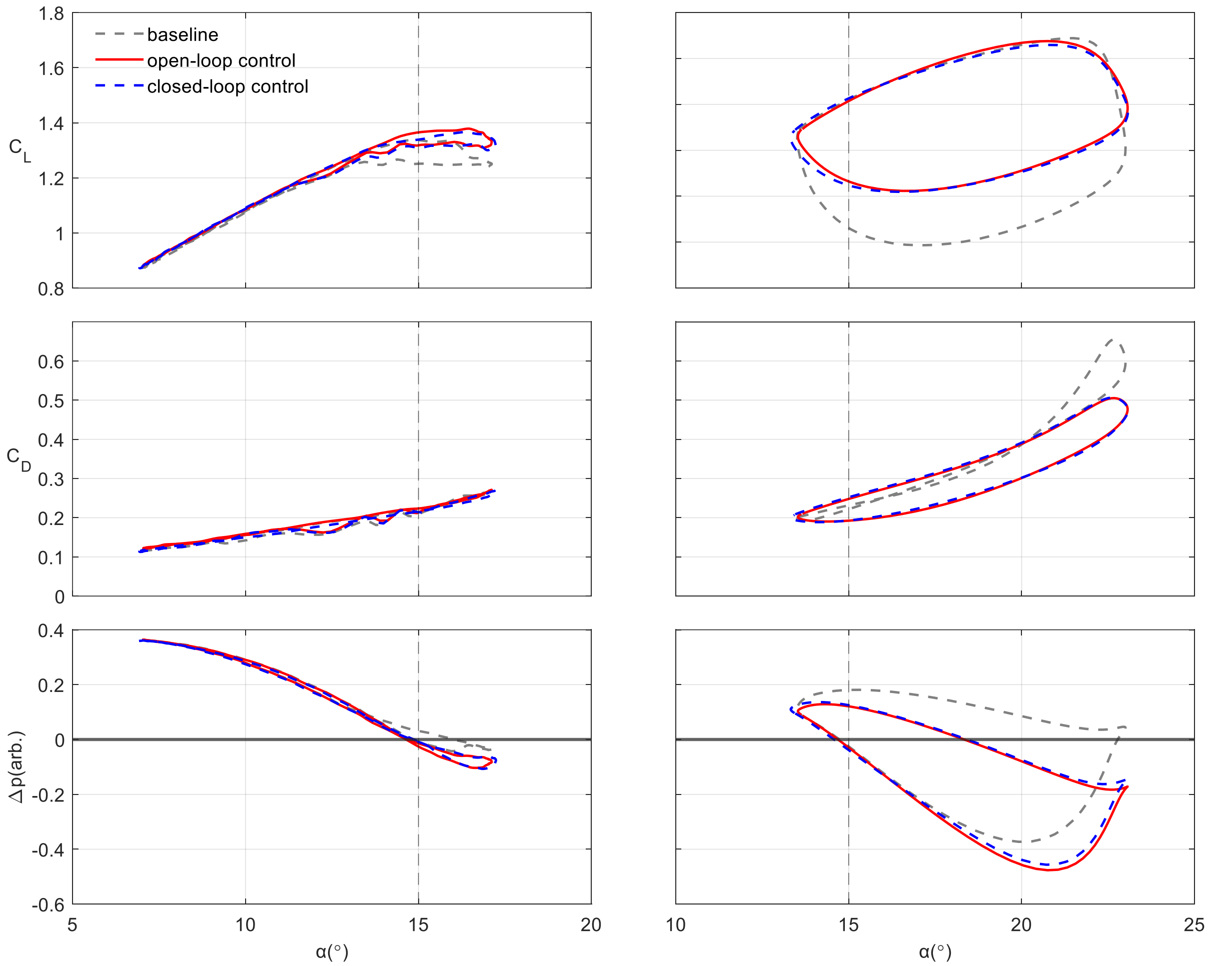

Fig. 11. Phase-averaged baseline, open-loop and closed-loop aerodynamic coefficients and leading-edge pressure with $\bar{\alpha} = 12°$ and $k = 0.01$ (left); and $\bar{\alpha} = 18°$ and $k = 0.1$ (right).

The main difference between closed- and open-loop control occurs close to the static stall angle during the pitch-up motion. This is most clearly seen at the lowest pitch rate in Fig. 8 and Fig. 11 (left-hand columns) and is a direct consequence of pulsation initiation at an angle slightly greater than the stall angle. At higher pitchrates, namely $k = 0.05$ and $k = 0.1$, this difference becomes smaller due to the lift overshoot, namely the delayed response of the boundary layer separation, relative to the time-scales associated with the pitching motion. As mentioned above, the angle-of-attack corresponding to the leading-edge pressure zero crossings during pitch-down motion increases with increasing pitchrate. This means that closed-loop pulsations are terminated at angles of attack substantially larger than the static stall angle. Despite this, the lift and drag coefficients are essentially identical to those obtained with open-loop control. There are two reasons for this. First, the system dead-time of between 20 to 50 milliseconds delays initiation, although this accounts for an angle-of-attack less than one degree. Second, flow separation following termination occurs over more than 10 convective time units, i.e., $t_{sep}U_\infty / c > 10$ [24], which corresponds to approximately 300 milliseconds. In simple terms, the time taken for a boundary layer to separate following termination is at least an order of magnitude greater than the time taken for the wing to pitch down from the pressure zero-crossing time to the static stall angle. A similar observation was made when studying dynamic stall on vertical axis wind turbines, where plasma actuation during pitch-up of the blades produced a similar result to continuous (open loop) pulse-modulation [25].

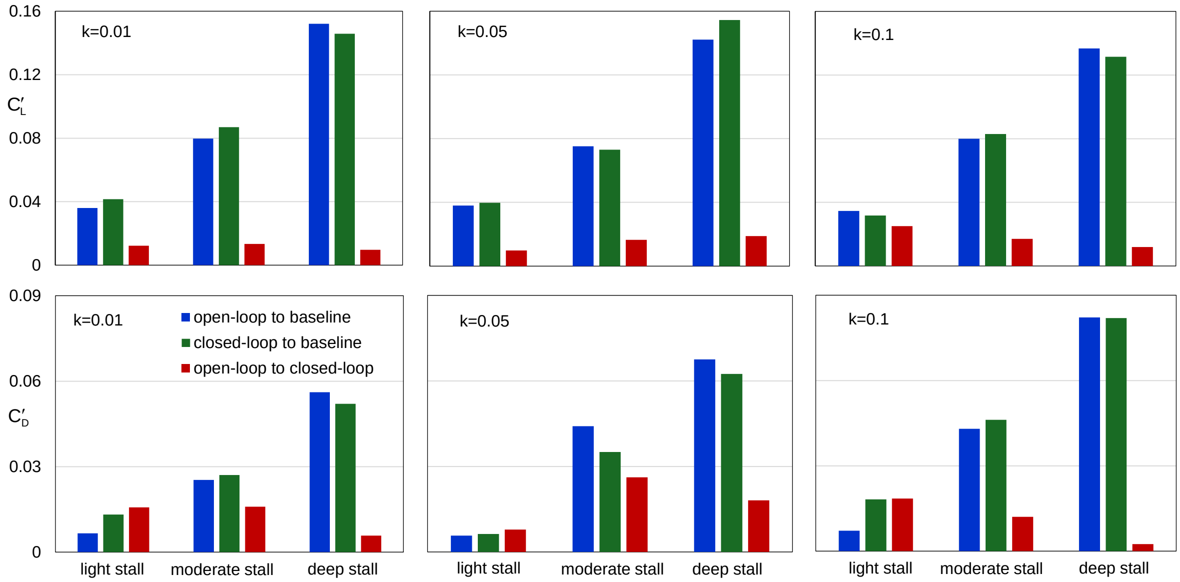

Fig. 12. Root-mean-square of the differences between controlled and baseline cases for all harmonic pitching conditions studied.

The lift coefficient results from all harmonic pitching cases are summarized by calculating the root-mean-square of the differences between open-loop control and baseline (o-b) cases:

$$C'_{L,\text{o-b}} = \left(\frac{1}{N} \sum_{i=1}^{N} \left(C_{L,\text{o}} - C_{L,\text{b}} \right)_i^2 \right)^{1/2} \tag{2}$$

closed-loop control and baseline (c-b) cases:

$$C'_{L,\text{c-b}} = \left(\frac{1}{N} \sum_{i=1}^{N} \left(C_{L,\text{c}} - C_{L,\text{b}} \right)_i^2 \right)^{1/2} \tag{3}$$

the closed- and open-loop control (c-o) cases:

$$C'_{L,\text{c-o}} = \left(\frac{1}{N} \sum_{i=1}^{N} \left(C_{L,\text{c}} - C_{L,\text{o}} \right)_i^2 \right)^{1/2} \tag{4}$$

Identical root-mean-square calculations were conducted for the corresponding drag coefficients and a summary of all results is presented in Fig. 12. In general, the differences between $C'_{L,\text{o-b}}$ and $C'_{L,\text{c-b}}$ are small, never exceeding 0.012, and $C'_{L,\text{c-o}}$ never exceeds 0.025. Thus, the main conclusion is that the closed-loop control system implemented here is effective. The small differences are due to the pressure zero-crossing being slightly greater than the static stall angle and the experimental uncertainty. The sensing method can easily be improved by (i) changing the threshold pressure, (ii) integrating the actuator into the airfoil geometry [15,18] or by moving the pressure sensor further upstream. This latter option proved to be difficult due to the technical difficulty encountered due to the presence of the actuator. However, on a large (up scaled) wing this problem is easily ameliorated, because the width of the actuator does not scale with the wind chord-length.

D. Unsteady Pitch-and-Hold Experiments

Baseline, open-loop and closed-loop control experiments for unsteady pitch-and-hold motion were conducted in a similar manner to the harmonic pitching motion experiments described in section III.C. Both pitch-up and pitch-down motions were prescribed by half-sine-waves, followed by a constant angle-of-attack. Formally, for pitch-up-and-hold motion:

$$\alpha = \bar{\alpha} + 5^\circ \sin\left(\frac{2kU_\infty t'}{\bar{c}} - \frac{\pi}{2} \right) \quad \text{for} \quad 0 \le t' \le \frac{\pi}{2} \frac{\bar{c}}{kU_\infty} \tag{5}$$

and

$$\alpha = \bar{\alpha} + 5^\circ \qquad \text{for} \qquad t' > \frac{\pi}{2}\frac{\bar{c}}{kU_\infty} \tag{6}$$

and for pitch-down-and-hold motion:

$$\alpha = \bar{\alpha} + 5^\circ \sin\left(\frac{2kU_\infty t'}{\bar{c}} + \frac{\pi}{2}\right) \qquad \text{for} \qquad 0 \le t' \le \frac{\pi}{2}\frac{\bar{c}}{kU_\infty} \tag{7}$$

$$\alpha = \bar{\alpha} - 5^\circ \qquad \text{for} \qquad t' > \frac{\pi}{2}\frac{\bar{c}}{kU_\infty} \tag{8}$$

where the time variable $t' = t - t_0$ is referenced to an arbitrary t_0 following steady state conditions. Ensemble-averaged results for light, moderate and deep stall are presented in Fig. 13, Fig. 14, and Fig. 15, respectively. For these representations, $t_0 = 0.5$ seconds for pitch-up motion and $t_0 = 14$, 6.5, and 5 seconds, for $k = 0.01$, 0.05 and 0.1 for pitch-down motion, respectively.

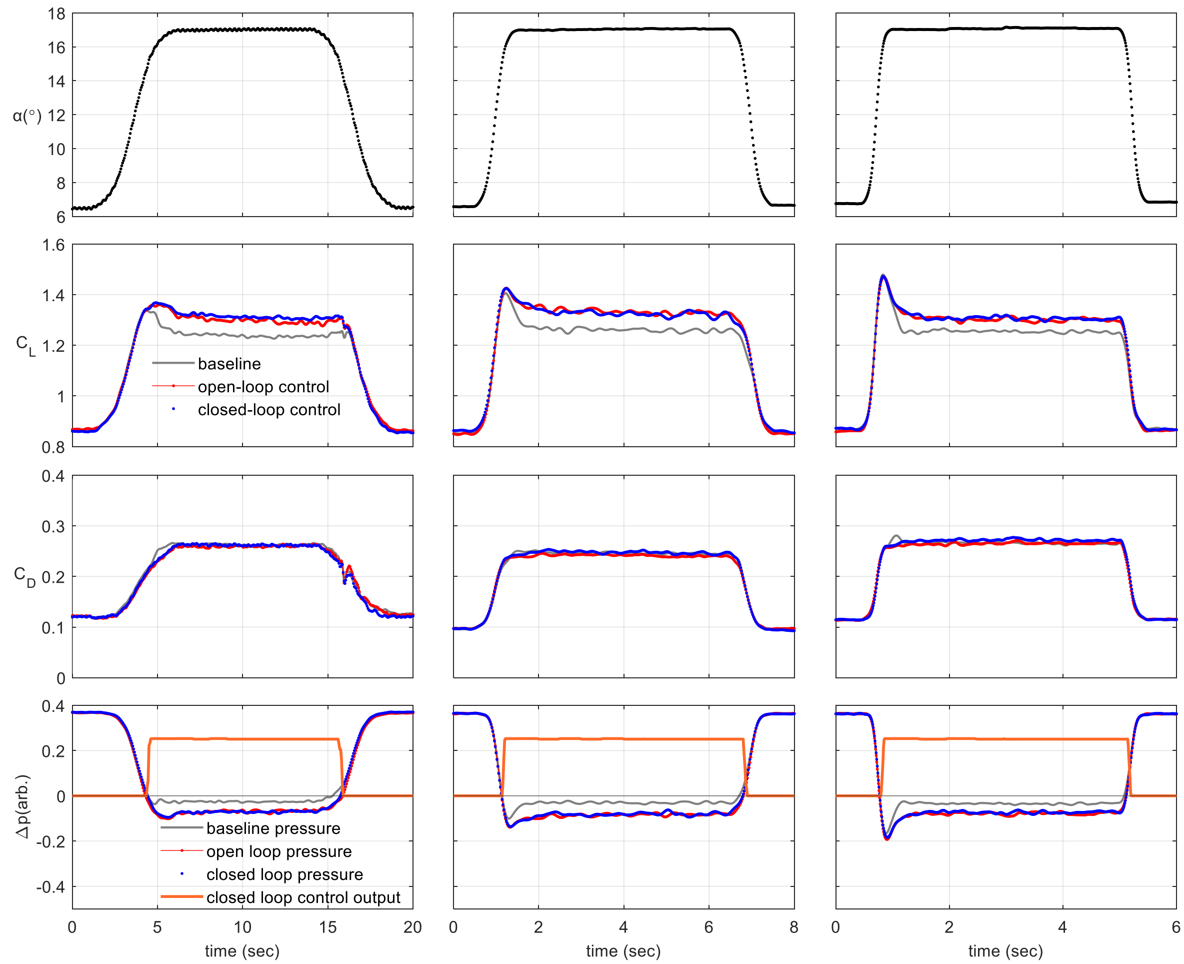

Fig. 13. Summary of light stall pitch-and-hold ensemble-averaged results for $k = 0.01$ (left), $k = 0.05$ (center), and $k = 0.1$ (right).

For all stall scenarios and pitchrates, open- and closed-loop results are virtually indistinguishable, to within experimental uncertainty, and hence the discussions relating to the actuated cases applies to both. In all cases, higher pitch-up rates result in greater overshoot of the static maximum lift, and actuation has a successively smaller effect on the maximum. The accompanying successively lower leading-edge pressures, at corresponding angles, are consistent with greater local inboard circulation. For the light stall scenario (Fig. 13), there is very little difference between the baseline and actuated pitch-down mechanisms, due to the attached leading-edge flow, indicated by the relatively high post-stall lift coefficients.

For the moderate and deep stall scenarios (Fig. 14 and Fig. 15), pitch-down produces a lift "undershoot" at the two higher baseline pitchrates. The source of this undershoot is most likely the shedding of a leading-edge vortex, that subsequently forms a stagnation region on the upper surface. Similar observations were made on a deflected flap following the initiation of zero mass-flux perturbations [24]. It can be hypothesized that this is, at least in part, a non-circulatory unsteady contribution to lift, due to the weak circulatory response associated with the leading-edge pressures. For moderate stall, the formation of the vortex is eliminated by actuation at $k = 0.05$ (Fig. 14, center), but in contrast, for deep stall at the same reduced frequency (Fig. 15, center), actuation appears to promote its formation. Under moderate and deep stall at $k = 0.1$, it is merely shifted to higher lift coefficients. Without surface pressure or flowfield measurements any attempt to explain these observations is purely speculative, although the dominant factor is the leading-edge initial condition prior to the pitch-down motion. For example, the baseline leading-edge pressures prior to pitch-down are either negative or positive, for the moderate ($\alpha_{max} = 20°$) and deep ($\alpha_{max} = 23°$) stall scenarios. This indicates leading-edge stall for the latter scenario and therefore a different pitch-dependent response. The differences between the actuated moderate and deep stall scenarios are more difficult to explain, because the initial conditions are nominally similar. Both surface pressure and flowfield measurements—for example particle image velocimetry—would be required to better understand these loading phenomena.

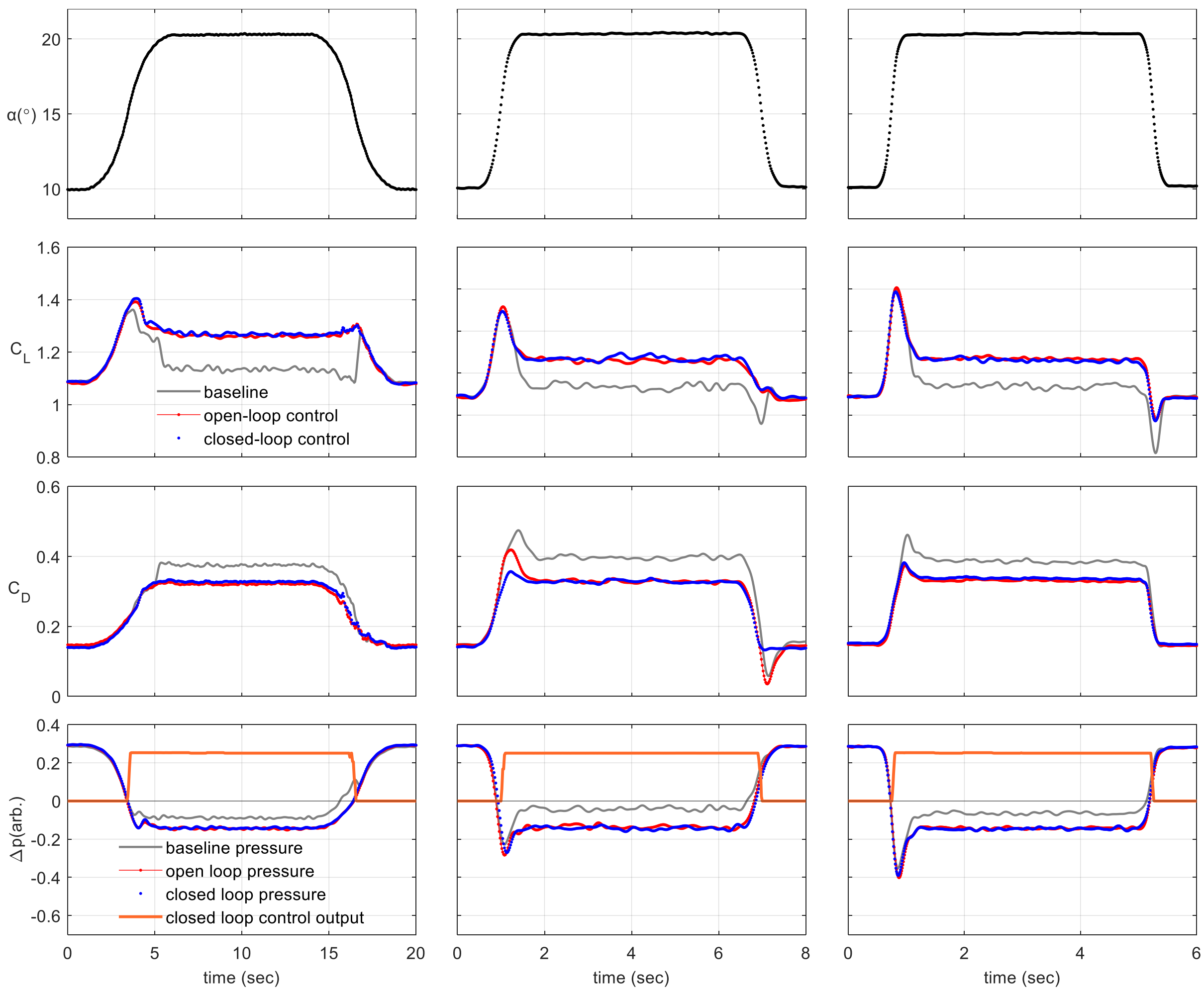

Fig. 14. Summary of moderate stall pitch-and-hold ensemble-averaged results for $k = 0.01$ (left), $k = 0.05$ (center), and $k = 0.1$ (right).

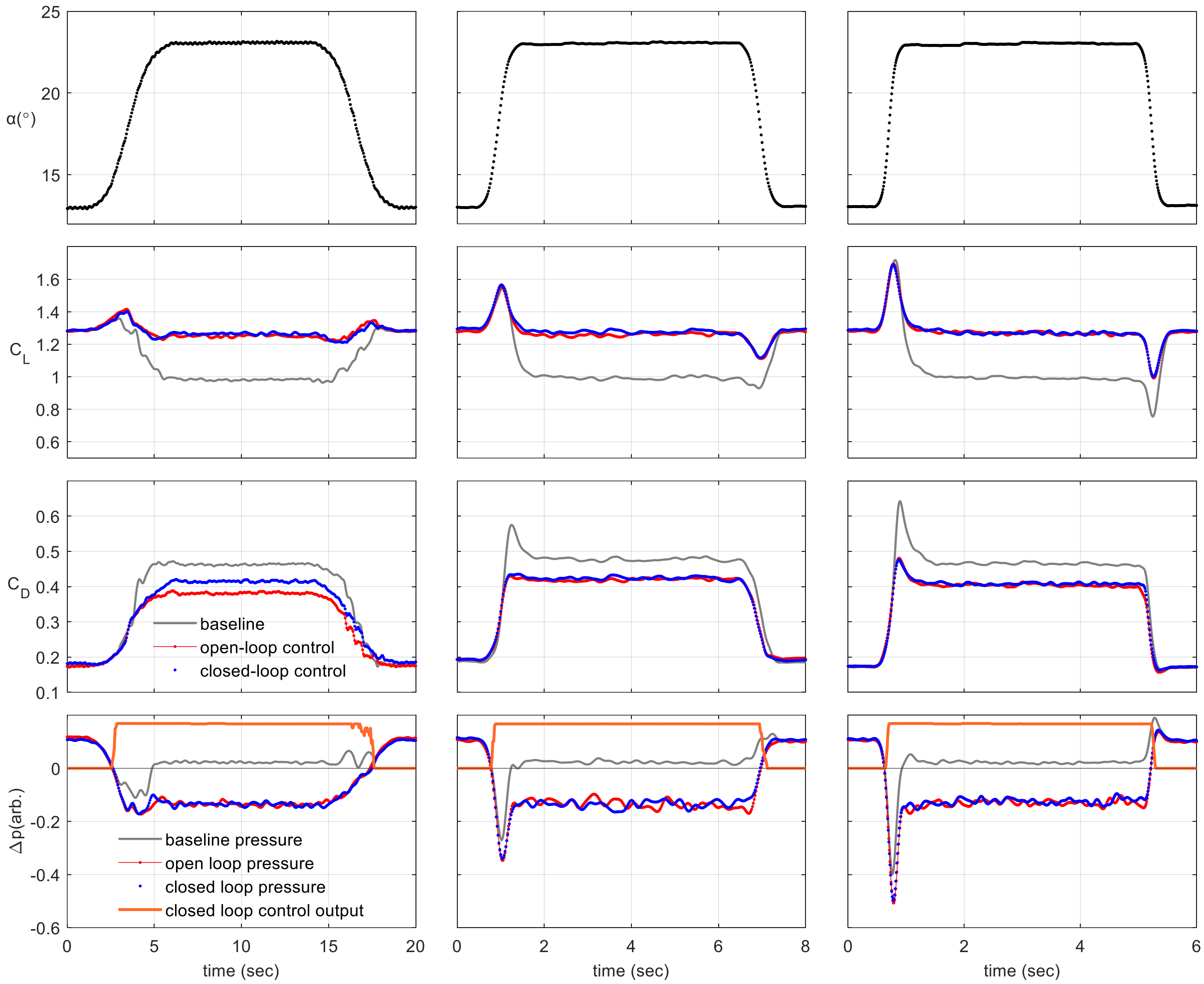

Fig. 15. Summary of deep stall pitch-and-hold ensemble-averaged results for $k = 0.01$ (left), $k = 0.05$ (center), and $k = 0.1$ (right).

IV. Conclusions

A closed-loop DBD plasma stall control system was demonstrated in a wind tunnel on a scale-model wing, based on pressure sensing below the leading-edge to initiate or terminate pulse-modulation. The present implementation was inspired by stall warning systems implemented on many GA aircraft and the actuation scheme effectively prevents leading-edge stall. The high-voltage electronics and battery were identical to a system evaluated on a flight model. The system was designed based on static data and was then evaluated dynamically, by both harmonic pitching of the wing, and pitch-and-hold motions. A wide range of angles-of-attack, from light-stall to deep-stall, was considered at reduced frequencies between 0.01 and 0.1, for both periodic sinusoidal and pitch-and-hold motions. The evaluation was conducted by comparing open-loop (continuous pulse-modulation) and closed-loop lift and drag coefficient. For all conditions considered, the differences between open- and closed-loop coefficients were small and ascribed to experimental error, thereby demonstrating the effectiveness and robustness of the system.

A welcome result was that even when pulsations were terminated at post-static-stall angles during pitch-down motion, no measurable differences between open- and closed loop control were observed. The reason for this is that the process of flow separation occurs over at least 10 convective time units, which is at least an order-of-magnitude larger than the time-interval between the zero-crossing angle and the static stall angle. In other words, the time taken for the boundary layer to separate following termination of the pulsations was at least an order of magnitude greater than the time that the wing exceeds the stall angle.

In light of the fact that scoop-based stall warning systems already exist on many GA aircraft, it is recommended to evaluate the system on a full-scale wing, or in flight. The thickness of the actuator which is less than 1 mm is unlikely to affect cruise performance significantly.

References

1. Anderson, J.D., "Introduction to Flight," 8th Edition, McGraw-Hill Education, New York, 2006, pp. 522-530.
2. Ellis, D.R. and Steinberger, J., "A study of lightplane stall avoidance and suppression," Department of Transportation, Federal Aviation Administration, System Research & Development Service, 1977.
3. https://www.aopa.org/-/media/files/aopa/home/pilot-resources/safety-and-proficiency/accident-analysis/special-reports/stall_spin.pdf
4. Fala, N., "An analysis of fixed-wing stall-type accidents in the United States," *Aerospace*, Vol. 9, No. 4, 2022, p. 178.
5. Torenbeek, E., "An introduction to wing design. In: Synthesis of subsonic airplane design," Springer, Dordrecht, 1982. https://doi.org/10.1007/978-94-017-3202-4_7.
6. Lin, J.C., "Review of research on low-profile vortex generators to control boundary-layer separation," *Progress in Aerospace Sciences*, Vol. 38, Issues 4-5, 2002, pp. 389-420.
7. Fouatih, O.M., Imine, B. and Medale, M., "Numerical/experimental investigations on reducing drag penalty of passive vortex generators on a NACA 4415 airfoil," *Wind Energy*, Vol. 22, No. 7, pp. 1003-1017.
8. Quackenbush, T., McKillip, R. and Whitehouse, G., "Development and testing of deployable vortex generators using SMA actuation," 28th AIAA Applied Aerodynamics Conference, p. 4686, 2010.
9. Nissle, S., Kaiser, M., Hübler, M., Gurka, M. and Breuer, U., "Adaptive vortex generators based on active hybrid composites: from idea to flight test," *CEAS Aeronautical Journal*, Vol. 9, 2018, pp. 661-670.
10. Morice, S.D., Ginnell, K., Geary, S., Baughn, J. and Robinson, S.K., "Detection of boundary layer separation and implementation of autonomous vortex generators," AIAA Scitech 2020 Forum, 2020, p. 0788.
11. Müller-Vahl, H., Nayeri, C.N., Paschereit, C.O. and Greenblatt, D., "Dynamic stall control via adaptive blowing," *Renewable Energy*, Vol. 97, 2016, pp. 47-64.
12. Greenblatt, D. and Wygnanski, I., "The control of separation by periodic excitation," *Progress in Aerospace Sciences*, Volume 36, Issue 7, 2000, pp. 487-545.
13. Hansen, L. and Bons, J., "Flow Measurements of vortex generator jets in separating boundary layer," *Journal of Propulsion and Power*, Vol. 22, No. 3, 2006, pp. 558-566. https://doi.org/10.2514/1.13820.
14. Corke, T.C., Post, M.L., and Orlov, D.M., "SDBD plasma enhanced aerodynamics: concepts, optimization and applications," *Progress in Aerospace Sciences*, Vol. 43, 2007, pp. 193-217.
15. Kelley, C.L., Bowles, P.O., Cooney, J., He, C., Corke, T.C., Osborne, B.A., Silkey, J.S. and Zehnle, J., "Leading-edge separation control using alternating-current and nanosecond-pulse plasma actuators," *AIAA Journal*, Vol. 52, No. 9, pp. 1871-1884, 2014.
16. Keisar, D., Hasin, D. and Greenblatt, D., "Plasma actuator application on a full-scale aircraft tail," *AIAA Journal*, Vol. 57, No. 2, 2019, pp. 616-627. http://dx.doi.org/10.2514/1.J057233.
17. Greenblatt, D., Göksel, B., Rechenberg, I., Schüle, C., Romann, D. and Paschereit, C.O., "Dielectric barrier discharge flow control at very low flight Reynolds numbers," *AIAA Journal*, Vol. 46, No. 6, 2008, pp. 1528-1541. https://doi.org/10.2514/1.33388.
18. De Troyer, T., Hasin, D., Keisar, D., Santra, S. and Greenblatt, D., "Plasma-based dynamic stall control and modelling on an aspect-ratio-one wing," *AIAA Journal* Vol. 60, No. 5, 2022, pp. 2905-2915. https://doi.org/10.2514/1.J060933.
19. Lombardi, A.J., Bowles, P.O. and Corke, T.C., "Closed-loop dynamic stall control using a plasma actuator," *AIAA Journal*, Vol. 51, No. 5, 2013, pp. 1130-1141. https://doi.org/10.2514/1.J051988.
20. Zalovcik, J.A., "Summary of stall-warning devices," NACA-TN-2676, 1952.
21. Garcia M. and Greenblatt, D., "Mini UAV with DBD-plasma-based flow control," AIAA Aviation 2023 Forum, p. 4306, 2023.
22. Greenblatt, D., "Unsteady low-speed wind tunnels," *AIAA Journal*, Vol. 54, No. 6, 2016, pp. 1817-1830. https://doi.org/10.2514/1.J054590.
23. Post, M.L. and Corke, T.C., "Separation control using plasma actuators: dynamic stall vortex control on oscillating airfoil, *AIAA Journal*, Vol. 44, No. 12, 2006, pp. 3125-3135. http://dx.doi.org/10.2514/1.22716.
24. Greenblatt, D., Nishri, B., Darabi, A. and Wygnanski, I., "Dynamic stall control by periodic excitation, Part 2: Mechanisms," *Journal of Aircraft*, Vol. 38, No. 3, 2001, pp. 439-447.
25. Ben-Harav, A. and Greenblatt, D., "Plasma-based feed-forward dynamic stall control on a vertical axis wind turbine," *Wind Energy*, Vol. 19, No. 1, 2016, pp. 3-16.

View publication stats